

Robust quantized transport from topological quasienergy winding in long-range-coupling synthetic quantum walks

Chengzhi Qin^{1,#}, Yinglan Li^{1,#}, Bing Wang^{1,*}, Zimeng Zou¹, Jiaxin Xu¹, Xinyuan Hu¹,

Alberto Amo^{2,*} and Peixiang Lu^{1,3,*}

¹*School of Physics and Wuhan National Laboratory for Optoelectronics, Huazhong University of Science and Technology, Wuhan 430074, China.*

²*Univ. Lille, CNRS, UMR 8523—PhLAM—Physique des Lasers Atomes et Molécules, F-59000 Lille, France*

³*Hubei Key Laboratory of Optical Information and Pattern Recognition, Wuhan Institute of Technology, Wuhan 430205, China.*

These authors contributed equally: Chengzhi Qin and Yinglan Li

*Corresponding authors:

B.W. (email: wangbing@hust.edu.cn),

A. A. (email: alberto.amo-garcia@univ-lille.fr),

P. L. (email: lupeixiang@hust.edu.cn).

Abstract

Quantized transport is a prominent feature in topological physics, with canonical examples being the quantum Hall effect and adiabatic Thouless pump, which are based on the Chern number, a topological invariant of 2D systems. Going beyond the Chern-number-based paradigms, quantized transports can also arise from k -direction quasienergy winding unique to periodically driven (Floquet) systems, which are free of dimensionality and adiabaticity limitations. However, lattices displaying winding of their quasienergy bands require asymmetric long-range couplings that are difficult to achieve in lattices of real-space coupled sites. Here, by leveraging photonic synthetic dimensions we construct asymmetric long-range-couplings in a one-dimensional temporal quantum walk based on three coupled fiber loops. We demonstrate quantized transport arising from the winding of quasienergy bands in k direction. We show that the average group velocity of an initial wave packet is proportional to the winding number, which leads to a quantized transport displacement. To better visualize this quantized displacement, we cascade two regions with flipped nearest/long-range couplings and observe a focusing effect with a quantized spatial shift in the focusing point. We also probe the robust properties of quantized transport against obstacles and disorders. The study initiates quasienergy-winding-based topological transports, which can feature applications in precise and robust imaging and information processing.

Introduction

Quantized transport is a prominent bulk signature in topological physics. A canonical example is the quantum Hall effect (QHE)¹ manifesting as the quantization of Hall conductance, with the quantized value given by a topological invariant of the Chern number². Another celebrated example is Thouless pump showing quantized charge transport due to adiabatic cyclic variation of system Hamiltonian³⁻⁸. The pumped charge per cycle is also expressed by the Chern number defined over an effective 2D Brillouin zone (BZ) formed by momentum k and time t , making Thouless pump a 1D dynamic version of 2D QHE. Since Chern number is defined using eigenfunctions via a 2D integral of the Berry curvature, the quantized transports in QHE and Thouless pump are both eigenfunction-based topological effects, which are typically restricted to 2D systems.

Going beyond above eigenfunction-based topological quantized transports, various interests have also been paid to periodically driven (Floquet) systems⁹⁻¹⁷. Without using the information of eigenfunctions, Floquet systems possess a unique topological property associated to the winding of quasienergy¹⁰⁻¹³ (see Fig. 1a for physical picture), which has no counterparts in static systems. Unlike Thouless pump relying on adiabatic change of 1D lattice Hamiltonian, nontrivial quasienergy winding can lead to topological effects free of adiabaticity and dimensionality limitations, such as quantized transports in 1D and higher dimensional systems¹⁰ (see Fig. 1b for a schematic illustration in 1D) irrespective of the value of the underlying Chern number. Since periodic driving is a universal protocol, Floquet topological effects can arise in many different settings from condensed matter, atomic to photonic and acoustic systems¹⁴⁻¹⁷. Photonic systems provide a versatile testbed to simulate Floquet topological effects, ranging from Thouless pump in 1D periodically driven waveguide arrays^{7, 8, 18} to Floquet topological insulators in 2D helical waveguide arrays¹⁹. However, the featured quantized transport arising from nontrivial quasienergy winding hasn't been realized yet.

Recently, a photonic quantum walk with broken inversion symmetry has been proposed to manifest nontrivial quasienergy winding along a parametric dimension^{20,21}, leading to the topological Bloch oscillations with sub-oscillation times linked to the winding number. Analogously, to induce k -direction quasienergy winding (Fig. 1a) and, consequently, quantized real-space transport, spatial inversion symmetry needs to be broken by introducing asymmetric long-range hopping orders²⁰. These couplings bias the transport of particles towards one direction of the lattice, in a similar manner to the

effect of the non-Hermitian asymmetric hopping amplitudes in the Hatano-Nelson model²²⁻²⁵. However, asymmetric long-range couplings are difficult to achieve using spatial lattices, making their experimental demonstrations elusive to date.

In this work, we propose a long-range-coupling temporal quantum walk and experimentally demonstrate quantized transport from k -direction quasienergy winding. Synthetic temporal quantum walks created using double fiber loops have emerged recently as privileged platforms²⁵⁻²⁸ to emulate various photonic topological effects, ranging from topological triple phase transition²⁹, momentum-gap topology³⁰ to space-time topology³¹ and extrinsic topology³². Here, by extending the traditional double fiber-loop structure to a triple fiber-loop with precisely controlled loop lengths, we introduce asymmetric long-range couplings into the quantum walk, which generate a ramped term in the Floquet band structure resulting in the winding of quasienergy along the k direction. When injecting a spatially symmetric wave packet, we find that the weighted average group velocity over the BZ is proportional to this winding number, leading to a quantized mean displacement of the packet in one Floquet period. We measure this quantized displacement by extracting the center-of-mass (COM) for three different long-range coupling orders. By cascading two regions with flipped nearest/long-range couplings, we also achieve a focusing effect with quantized shifted focusing point, showing a better way to visualize the quantized displacement. We also observe the strong robust properties of quantized transport against specific obstacles and disorders. Finally, we generalize the quantum walk from a two-step to a multi-step Floquet driving protocol and achieve more universal quantized transport featuring arbitrarily large winding number.

Results

Theoretical model of quasienergy-winding-induced quantized transport

Consider the pulse evolution in three-coupled fiber loops consisting of a shorter loop A with length L_A and two longer B/C loops with lengths L_B/L_C (Fig. 1c). By designing $(L_C - L_A)/(L_B - L_A) = (r+1)/(1+1)$ with $r \in \mathbb{Z}$ and making the pulses pass through B/C loops at odd/even steps, one can create a quantum walk in a synthetic 1D temporal dimension with alternate rightward nearest/ r th-order long-range couplings at successive time steps of the walk, as schematized in Fig. 1d. Due to the discrete translational symmetry along lattice (n) and evolution (m) directions, the system can be described by

Floquet-Bloch theory. A complete Floquet period consists of two steps, each containing light scattering at the node described by a 2×2 scattering matrix S_i , in which the input-output ports correspond to pulses of light in the A and B/C loops. The scattering is followed by the leftward/rightward propagation links described by a shift operator $B_i(k)$, where $i = 1, 2$ denotes odd and even steps. The momentum-space Floquet operator is thus $U_F(k) = [B_2(k)S_2][B_1(k)S_1]$, with $B_2(k) = \begin{pmatrix} e^{ik/2} & 0 \\ 0 & e^{-irk/2} \end{pmatrix}$, $B_1(k) = \begin{pmatrix} e^{ik/2} & 0 \\ 0 & e^{-ik/2} \end{pmatrix}$, $S_i = \begin{pmatrix} \cos(\beta_i) & i \sin(\beta_i) \\ i \sin(\beta_i) & \cos(\beta_i) \end{pmatrix}$, where k is Bloch momentum, r is the long-range coupling order, β_i is the node's coupling angle, corresponding to a splitting ratio of $\cos^2(\beta_i)/\sin^2(\beta_i)$ for central variable optical coupler. The more general case in the presence of modulation phases along the propagation links is discussed in Supplementary Section 1.

By diagonalizing $U_F(k)$, we can obtain the Floquet band structure (see Supplementary Section 1 for detailed derivation)

$$\varepsilon_{\pm}(k) = \pm \cos^{-1} \left\{ \cos(\beta_2) \cos(\beta_1) \cos \left[\frac{(r+3)k}{4} \right] - \sin(\beta_2) \sin(\beta_1) \cos \left[\frac{(r-1)k}{4} \right] \right\} + \frac{(r-1)k}{4}, \quad (1)$$

Clearly, the band structure can be decomposed into a trigonometric (oscillatory) and a linear-function (ramped) part: $\varepsilon_{\pm}(k) = \pm t(k) + L(k)$, with $L(k) = (r-1)k/4$. The ramped term $L(k)$, as determined by the long-range coupling order r , induces quasienergy winding as k sweeps across the BZ (see Fig. 1a for the physical picture and Figs. 2a-2c for exemplified band structures with different windings). Such k -direction quasienergy winding can be characterized by a homotopy-class-based topological winding number, defined through the Floquet operator¹⁰⁻¹³

$$W_k = \frac{1}{2\pi} \int_{-K/2}^{K/2} dk \text{Tr}[U_F^{-1}(k) i \partial_k U_F(k)] = \frac{K}{2\pi} \frac{(r-1)}{2}, \quad (2)$$

where $K = 8\pi \text{lcm}[1/(r+3), 1/(r-1)]$ is the period of the BZ, lcm denotes the least common multiple. Since in our mesh-type lattice r can only take odd numbers, W_k is thus an integer. The physical meaning of W_k can also be identified from the Floquet band structure by counting the total times the two bands wind along the quasienergy axis as k runs over the BZ¹⁰⁻¹³. For example, for $r = 3, 5, 7$, we can calculate $K = 4\pi, 2\pi, 4\pi$, and $W_k = 2, 2, 6$ from Eq. (2), which can also be directly counted from Figs. 2a-2c.

Then, we connect the winding number to a physical observable of average transport displacement. A generic input state $|\psi_0\rangle$ can be decomposed into the superposition of all k components in the BZ, i.e.,

$|\psi_0\rangle = \int_{-K/2}^{K/2} c_+(k)|\psi_+(k)\rangle dk + \int_{-K/2}^{K/2} c_-(k)|\psi_-(k)\rangle dk$, where $|\psi_{\pm}(k)\rangle = [U_{\pm}(k), V_{\pm}(k)]^T e^{ikn/2}$ is the normalized eigenstate, $c_{\pm}(k) = \langle \psi_{\pm}(k) | \psi_0 \rangle$ is excitation coefficient at momentum k , corresponding to the excitation probability of $P_{\pm}(k) = |c_{\pm}(k)|^2$ with the normalization condition $\int_{-K/2}^{K/2} [P_+(k) + P_-(k)] dk = 1$. Since $P_{\pm}(k)$ is usually nonuniform but highly k -dependent, the transport displacement of the initial wave packet is described by the weighted average group velocity $\bar{v}_{gw} = \int_{-K/2}^{K/2} [P_+(k)v_{g,+}(k) + P_-(k)v_{g,-}(k)] dk$, where $v_{g,\pm}(k) \equiv \partial \varepsilon_{\pm}(k) / \partial k$ is the group velocity in each band at momentum k . Performing the decomposition $v_{g,\pm}(k) \equiv \partial [L(k) \pm t(k)] / \partial k = (r-1)/4 \pm v_{g,t}(k)$, with $v_{g,t}(k) \equiv \partial t(k) / \partial k$, yields $\bar{v}_{gw} = \frac{r-1}{4} + \int_{-K/2}^{K/2} P_+(k)v_{g,t}(k) dk - \int_{-K/2}^{K/2} P_-(k)v_{g,t}(k) dk$. Quantized transport requires $\bar{v}_{gw} = \frac{r-1}{4}$, which further requires $\int_{-K/2}^{K/2} P_{\pm}(k)v_{g,t}(k) dk = 0$. Since \bar{v}_{gw} plays the role of average phase accumulation rate (slope) of each band, the two bands accumulate the total phase of $W_k(2\pi)$ as k runs over the BZ, $W_k(2\pi) = (2\bar{v}_{gw})K$, which gives rise to a total average group velocity of $2\bar{v}_{gw} = \frac{2\pi W_k}{K}$ in one Floquet period. After P Floquet periods, we can obtain a quantized transport displacement

$$\Delta n = (2\bar{v}_{gw})P = \left(\frac{r-1}{2}\right)P = \left(\frac{2\pi W_k}{K}\right)P. \quad (3)$$

The condition $\int_{-K/2}^{K/2} P_{\pm}(k)v_{g,t}(k) dk = 0$ can be satisfied by choosing an appropriate input state $|\psi_0\rangle$.

This can be fulfilled by choosing the initial wave packet $|\psi_0\rangle = (1, \pm 1)^T$ located at a single lattice site with equal amplitudes in the short/long loops and either 0 or π phase difference. In Supplementary Section 2 we discuss the general cases in which the quantized transport condition can be achieved in the presence of gauge potentials added to the lattice using additional phase modulators.

Experimental demonstration

We build a triple fiber-loop circuit to verify above quantized transport effect. We select three simplest long-range coupling orders $r = 3, 5, 7$ by choosing loop lengths $L_A \sim 5\text{km}$, $L_B \sim 5\text{km} + 35\text{m}$, and $L_C \sim 5\text{km} + 70\text{m}$, $5\text{km} + 105\text{m}$, $5\text{km} + 140\text{m}$, corresponding to $(L_C - L_A) / (L_B - L_A) = (r+1) / (1+1) = 2, 3, 4$. More precise control over the loop lengths is achieved by measuring pulse intervals and using fiber segments to compensate for the extra required lengths. To ensure vanishing phase shifts along the paths, we turn off all phase modulators (PMs) and compensate for the length-mismatch induced extra phase.

We also use Erbium-doped fiber amplifiers (EDFAs) and acousto-optic modulators (AOMs) to attain equal gain/loss rates in the three loops. The single-site input condition $|\psi_0\rangle = (1, \pm 1)^T$ is attained by adopting two preprocessed steps with controlled amplitude and phase. More details about above key techniques are discussed in the Methods part.

Figures 2a-2c show the calculated Floquet band structures for $r = 3, 5, 7$ under $\beta_{1,2} = 0.47\pi$, all showing quasienergy winding with $K = 4\pi, 2\pi, 4\pi$ and $W_k = 2, 2, 6$. The calculated $P_{\pm}(k)$ and $v_{g,t}(k)$ for the three cases are shown in Figs. 2d-2f, all manifesting as even and odd function in the BZ to fulfill $\int_{-K/2}^{K/2} P_{\pm}(k)v_{g,t}(k)dk = 0$. The measured diffraction patterns under single-site $|\psi_0\rangle = (1, 1)^T$ input are depicted in Figs. 2g-2i. Yellow circles denote the extracted beam's COM, $n_{\text{COM}}(m) = \sum_n n(|u_n^m|^2 + |v_n^m|^2) / \sum_n (|u_n^m|^2 + |v_n^m|^2)$, where $|u_n^m|^2, |v_n^m|^2$ are measured pulse intensities at position n and step m in A, B/C loops. The COM's displacements after $P = 10$ Floquet periods ($M = 2P = 20$ steps) are $\Delta n_{\text{exp}} = 9.97, 20.07, 30.05$, fairly in agreement with the theoretical quantized values of $\Delta n = P(r - 1)/2 = 10, 20, 30$.

To better visualize this quantized displacement, we further construct two cascaded regions with a temporal boundary locating at $m_b = M/2$, before and after which nearest/long-range couplings are flipped at odd/even steps, such that beam refraction will occur. The main effect of this change in the temporal protocol is to invert the occupations of the two bands at m_b resulting in a refocusing after m_b steps. To see this, consider an initial state $|\psi_i\rangle = c_+(k)|\psi_+(k)\rangle + c_-(k)|\psi_-(k)\rangle$ at momentum k incident from region 1, it will be projected onto the new eigenstates at k in region 2 due to the conservation of k (Snell's law), $|\psi_i\rangle = c'_+(k)|\psi'_+(k)\rangle + c'_-(k)|\psi'_-(k)\rangle$, where $|\psi_{\pm}(k)\rangle, |\psi'_{\pm}(k)\rangle$ are normalized eigenstates in regions 1 and 2 (see Supplementary Section 3 for their explicit formulas). By applying wavefunction continuity condition $|\psi_i\rangle = |\psi_i\rangle$ and orthonormal condition $\langle\psi'_{\pm}(k)|\psi'_{\pm}(k)\rangle = 1, \langle\psi'_{\pm}(k)|\psi'_{\mp}(k)\rangle = 0$, we can obtain the transfer matrix relating the band occupancies in the two regions, $[[c'_+(k)|^2, |c'_-(k)|^2]^T = \mathbf{T}[[c_+(k)|^2, |c_-(k)|^2]^T$, with

$$\mathbf{T} = \begin{pmatrix} T_{++}(k) & T_{+-}(k) \\ T_{-+}(k) & T_{--}(k) \end{pmatrix} = \begin{pmatrix} |\langle\psi'_+(k)|\psi_+(k)\rangle|^2 & |\langle\psi'_+(k)|\psi_-(k)\rangle|^2 \\ |\langle\psi'_-(k)|\psi_+(k)\rangle|^2 & |\langle\psi'_-(k)|\psi_-(k)\rangle|^2 \end{pmatrix}, \quad (4)$$

where T_{ij} ($i, j = \pm$) denotes the occupancy conversion efficiency from j to i band from region 1 to 2. One can check numerically that for $\beta_{1,2} \sim \pi/2$, $T_{++}(k) = T_{--}(k) = 0, T_{+-}(k) = T_{-+}(k) = 1$ for most k components, meaning complete band occupancy inversion for negative refraction (see Supplementary Section 3 for

detailed analysis). For a single-site input, complete band occupancy inversion for most k when traversing the temporal interface between the two regions will lead to beam focusing onto a single site, accompanied by a quantized displacement of Δn . Such focusing effect allows us to better visualize the quantized displacement since COM coincides with the focusing point. Figures 2j-2l show negative refraction processes for the three cases, all showing near-perfect focusing with $\Delta n_{\text{exp}} = 9.97, 20.05, 30.08$ that approach $\Delta n = 10, 20, 30$. This focusing effect with a quantized shifted displacement may find applications in precise image transfer and processing, etc.

Robustness properties of quantized transport against obstacles and disorders

Since quantized transport is associated to the topological winding number, it should possess robustness properties against certain perturbations and disorders. From the condition $\int_{-K/2}^{K/2} P_{\pm}(k)v_{g,t}(k)dk = 0$, we note that if we introduce symmetrically-distributed momentum filters with blocked regimes $\pm k_{\text{block}}$ into the BZ, quantized transport can still exist, with the condition modified to $\int_{-K/2, k \notin k_{\text{block}}}^{K/2} P_{\pm}(k)v_{g,t}(k)dk = 0$. According to Fourier analysis, the symmetrically-distributed filters in momentum space correspond to symmetrically-placed obstacles (with respect to the beam's COM) in real space. In the experiment, we use an AOM to create an absorption event to mimic an obstacle. Figures 3a and 3b depict $P_{\pm}(k)$ and $v_{g,t}(k)$ for $r = 7, \beta_{1,2} = \pi/4$. The presence of a symmetric obstacle (cyan block in Fig. 3d) doesn't change $P_{\pm}(k)$ and $v_{g,t}(k)$ but only introduces symmetric blocked intervals (cyan ribbons in Fig. 3b) satisfying $|v_{g,t}(k_{\text{block}})| \leq v_{\text{gm}}$, where v_{gm} is the group velocity upper bound reaching the edges of obstacle. In Figs. 3c-3e, we plot the measured single-site diffraction patterns for three cases: (i) without obstacle; (ii) with a symmetric obstacle in the regime $n_{\text{block}} = [n_{\text{COM}} - \Omega/2, n_{\text{COM}} + \Omega/2]$ at $m = M/2$ step, where n_{COM}, Ω are the center and width of obstacle; (iii) with a complementary, symmetric obstacle outside n_{block} . By choosing $\Omega = 16, M = 20$, we get $v_{\text{gm}} = \Omega/M = 0.8$, which is shown in Fig. 3b and marked by cyan dashed lines in Figs. 3d and 3e. For the three cases, we obtain quantized displacements of $\Delta n_{\text{exp}} = 29.89, 29.85, 30.15$, all approaching $\Delta n = 30$. Moreover, we show that the robustness properties are applicable to different types of obstacles, irrespective of their size, position and distribution as long as they are symmetric with respect to the beam's COM. As verified by the simulated results in Supplementary Section 4, we choose a narrower, a broader, periodically-distributed and combined obstacles and can all obtain quantized displacements.

Apart from being immune to obstacles, quantized transport is also robust against various disorders. Note that the winding number doesn't rely on β_1, β_2 [see Eq. (2)], which allows the perturbations in coupling angles. To check this, by choosing a randomly varying $\beta(m) = \beta_0 + \Delta\beta(m)$ (Fig. 3f), where $\beta_0 = 0.47\pi$, $\Delta\beta(m) \in [-0.03\pi, 0.03\pi]$ with a uniform probability, we still obtain quantized displacements of $\Delta n_{\text{exp}} = 30.06, 30.08$ (Figs. 3g and 3h) that both approach $\Delta n = 30$. We further prove that quantized transport is also robust against phase disorder that can be introduced into the fiber rings using phase modulators. As discussed in Supplementary Section 3, no constraints are imposed on the scalar potentials introduced by the modulators to achieve quantized transport since they only induce a constant quasienergy shift without affecting the winding properties of the lattice. As a result, quantized transport can be robust against any phase disorders in the form of scalar potentials. To verify this, we choose $r = 7, \beta_{1,2} = 0.47\pi$ and apply a randomly varying scalar potential by adding into short/long loops a common phase of $\varphi(m) \in [-\pi, \pi]$ with a uniform probability (Fig. 3j). We can still obtain quantized displacements of $\Delta n_{\text{exp}} = 30.08, 30.09$ that approach $\Delta n = 30$ (Figs. 3k and 3l).

We further argue that the robustness nature of quantized transport can enable applications in robust imaging, i.e., the reconstruction of arbitrary input states even in the presence of disorders. For the random $\beta(m)$ and $\varphi(m)$ cases, we input a symmetric and an asymmetric image (represented by multi-site inputs) and observe near-perfect imaging at output step, accompanied by quantized displacements of $\Delta n_{\text{exp}} = 30.07, 30.05$ (Figs. 3i and 3m) both approaching $\Delta n = 30$. These results prove that the imaging functionality is applicable to an arbitrarily input profile, highlighting its universal property.

Generalization to multi-step Floquet driving protocol with large winding number

Finally, we prove that quantized transport is a universal behavior applicable to the more general case with multi-step Floquet driving protocol, which also allows leftward long-range couplings. Consider a quantum walk with a Floquet period of T steps (even number $T = 2, 4, \dots$) and leftward, rightward coupling orders of l_i, r_i at the i -th step ($i = 1, 2, \dots, T$). The winding number is calculated as

$$W_k = \frac{K}{2\pi} \sum_{i=1}^T \left(\frac{r_i - l_i}{2} \right),$$

which is the general form of Eq. (2). (see Supplementary Section 5 for detailed derivation).

As a concrete example, we consider a four-step driving protocol with $l_i = 1, 1, 1, 1$ and $r_i = 1, r, r, r$,

r and $\beta_{1,2} = \beta$ (see Fig. 4a). The Floquet band structure is (see Supplementary Section 5 for derivation)

$$\begin{aligned} \varepsilon_{\pm}(k) = \pm \cos^{-1} & \left\{ [\cos(\beta)]^4 \cos\left[\frac{(3r+5)k}{4}\right] + [\sin(\beta)]^4 \cos\left[\frac{(r-1)k}{4}\right] \right. \\ & \left. - [\cos(\beta)\sin(\beta)]^2 \left\{ \cos\left[\frac{(3r+1)k}{4}\right] + 2\cos\left[\frac{(r-1)k}{4}\right] + 3\cos\left[\frac{(r+3)k}{4}\right] \right\} \right\} \\ & + \frac{3(r-1)k}{4}, \end{aligned} \quad (5)$$

which can also be decomposed into an oscillatory and a ramped term: $\varepsilon_{\pm}(k) = \pm t(k) + L(k)$, with $L(k) = 3(r-1)k/4$. The case for $r = 7$ is depicted in Fig. 4b, which shows $K = 4\pi$ and large winding number $W_k = 18$. The curves of $P_{\pm}(k)$ and $v_{g,t}(k)$ are depicted in Figs. 4c and 4d, which manifest as even and odd functions to fulfill $\int_{-K/2}^{K/2} P_{\pm}(k)v_{g,t}(k)dk = 0$, such that $\bar{v}_{gw} = \frac{\partial L(k)}{\partial k} = \frac{3(r-1)}{4} = \frac{9}{2}$. In our experiment, we study the evolution up to $P = 6$ Floquet periods ($M = 4P = 24$ steps) and obtain $\Delta n_{\text{exp}} = 53.93, 54.10$ (Figs. 4e and 4f), both in fairly agreement with the theoretical value of $\Delta n = (2\bar{v}_{gw})P = 54$. These results show that quantized transport allows more general Floquet driving protocol, which can enable an arbitrary large winding number.

Conclusion and outlook

In summary, we have demonstrated band-winding-induced quantized transport in long-range-coupling temporal quantum walks created in triple coupled fiber loops, where the long-range couplings generate a ramped term in the Floquet band structure to cause nontrivial quasienergy winding. We find the weighted average group velocity is proportional to this winding number, giving rise to the quantized transport effect. We observe quantized displacements for three long-range coupling orders of $r = 3, 5, 7$ and prove their robustness against certain obstacles and disorders. By cascading two regions with flipped nearest/long-range couplings, we also realize a beam focusing effect to better visualize this quantized displacement. The quantized transport can be generalized to quantum walks with multi-step driving protocol, which gives rise to arbitrarily large winding number.

Our experiment and analysis, done in a Floquet system under unitary evolution, go beyond tight binding lattice Hamiltonians and display interesting connections with non-Hermitian lattices²²⁻²⁵. It shows band-winding-induced topological transports with potential applications in precise yet robust information and image processing. This paradigm may stimulate further studies on topological

quantized transports in higher-dimensional quantum walks³³⁻³⁷, topological transports in the presence of nonlinearities³⁸⁻⁴⁰ or disorders⁴¹⁻⁴³. The combination of band-winding topology with eigenfunction-based topologies, such as momentum-gap topology^{31,32} or extrinsic topology³³ may enable compound topological effects, which are of peculiar interest for future studies.

Online content

Any methods, additional references, Nature Portfolio reporting summaries, source data, extended data, supplementary information, acknowledgements, peer review information; details of author contributions and competing interests; and statements of data and code availability are available at...

References

1. Klitzing, K. v., Dorda, G. & Pepper, M. New method for high-accuracy determination of the fine-structure constant based on quantized hall resistance. *Phys. Rev. Lett.* **45**, 494-497 (1980).
2. Thouless, D. J., Kohmoto, M., Nightingale, M. P. & den Nijs, M. Quantized Hall conductance in a two-dimensional periodic potential. *Phys. Rev. Lett.* **49**, 405-408 (1982).
3. Thouless, D. J. Quantization of particle transport. *Phys. Rev. B* **27**, 6083-6087 (1983).
4. Lohse, M., Schweizer, C., Zilberberg, O., Aidelsburger, M. & Bloch, I. A thouless quantum pump with ultracold bosonic atoms in an optical superlattice. *Nat. Phys.* **12**, 350-354 (2015).
5. Nakajima, S. et al. Topological thouless pumping of ultracold fermions. *Nat. Phys.* **12**, 296-300 (2016).
6. Lohse, M., Schweizer, C., Price, H. M., Zilberberg, O. & Bloch, I. Exploring 4D quantum Hall physics with a 2D topological charge pump. *Nature* **553**, 55-58 (2018).
7. Jürgensen, M., Mukherjee, S. & Rechtsman, M. C. Quantized nonlinear thouless pumping. *Nature* **596**, 63-67 (2021).
8. Jürgensen, M., Mukherjee, S., Jörg, C. & Rechtsman, M. C. Quantized fractional thouless pumping of solitons. *Nat. Phys.* **19**, 420-426 (2023).
9. Lindner, N. H., Refael, G. & Galitski, V. Floquet topological insulator in semiconductor quantum wells. *Nat. Phys.* **7**, 490-495 (2011).
10. Qi, X.-L., Hughes, T. L. & Zhang, S.-C. Topological field theory of time-reversal invariant

- insulators. *Phys. Rev. B* **78**, 195424 (2008).
11. Kitagawa, T., Berg, E., Rudner, M. & Demler, E. Topological characterization of periodically driven quantum systems. *Phys. Rev. B* **82**, 235114 (2010).
 12. Chiu, C.-K., Teo, J. C. Y., Schnyder, A. P. & Ryu, S. Classification of topological quantum matter with symmetries. *Rev. Mod. Phys.* **88**, 035005 (2016).
 13. Gao, Q. & Niu, Q. Floquet-Bloch oscillations and intraband Zener tunneling in an oblique spacetime crystal. *Phys. Rev. Lett.* **127**, 036401 (2021).
 14. Zhou, S. et al. Pseudospin-selective Floquet band engineering in black phosphorus. *Nature* **614**, 75-80 (2023).
 15. Eckardt, A. Colloquium: Atomic quantum gases in periodically driven optical lattices. *Rev. Mod. Phys.* **89**, 011004 (2017).
 16. Fleury, R., Khanikaev, A. B. & Alu, A. Floquet topological insulators for sound. *Nat. Commun.* **7**, 11744 (2016).
 17. Peng, Y.-G. et al. Experimental demonstration of anomalous Floquet topological insulator for sound. *Nat. Commun.* **7**, 13368 (2016).
 18. Cerjan, A., Wang, M., Huang, S., Chen, K. P. & Rechtsman, M. C. Thouless pumping in disordered photonic systems. *Light Sci. Appl.* **9**, 178 (2020).
 19. Rechtsman, M. C. et al. Photonic Floquet topological insulators. *Nature* **496**, 196-200 (2013).
 20. Upreti, L. K. et al. Topological swing of Bloch oscillations in quantum walks. *Phys. Rev. Lett.* **125**, 186804 (2020).
 21. Adiyatullin, A. F. et al. Topological properties of Floquet winding bands in a photonic lattice. *Phys. Rev. Lett.* **130**, 056901 (2023).
 22. Hatano, N. & Nelson, D. R. Localization transitions in non-Hermitian quantum mechanics. *Phys. Rev. Lett.* **77**, 570-573 (1996).
 23. Gong, Z. et al. Topological phases of non-Hermitian systems. *Phys. Rev. X* **8**, 031079 (2018).
 24. Bergholtz, E. J., Budich, J. C. & Kunst, F. K. Exceptional topology of non-Hermitian systems. *Rev. Mod. Phys.* **93**, 015005 (2021).
 25. Weidemann, S. et al. Topological funneling of light. *Science* **368**, 311-314 (2020).
 26. Monika, M. et al. Quantum state processing through controllable synthetic temporal photonic lattices. *Nat. Photon.* **19**, 95-100 (2024).

27. Qin, C. et al. Observation of discrete-light temporal refraction by moving potentials with broken Galilean invariance. *Nat. Commun.* **15**, 5444 (2024).
28. Qin, C. et al. Temporal Goos-Hänchen shift in synthetic discrete-time heterolattices. *Phys. Rev. Lett.* **133**, 083802 (2024).
29. Weidemann, S., Kremer, M., Longhi, S. & Szameit, A. Topological triple phase transition in non-Hermitian Floquet quasicrystals. *Nature* **601**, 354-359 (2022).
30. Ren, Y. et al. Observation of momentum-gap topology of light at temporal interfaces in a time-synthetic lattice. *Nat. Commun.* **16**, 707 (2025).
31. Feis, J., Weidemann, S., Sheppard, T., Price, H. M. & Szameit, A. Space-time-topological events in photonic quantum walks. *Nat. Photon.* **19**, 518-525 (2025).
32. Asapanna, R. et al. Observation of extrinsic topological phases in Floquet photonic lattices. *Phys. Rev. Lett.* **134**, 256603 (2025).
33. Chen, C. et al. Observation of topologically protected edge states in a photonic two-dimensional quantum walk. *Phys. Rev. Lett.* **121**, 100502 (2018).
34. Pang, Z., Abdelghani, O., Soljačić, M. & Yang, Y. Topological quantum walk in synthetic non-abelian gauge fields with photonic mesh lattices. *Optica* **12**, 1794-1799 (2025).
35. Muniz, A. L. M. et al. 2D solitons in PT-symmetric photonic lattices. *Phys. Rev. Lett.* **123**, 253903 (2019).
36. Lin, Q., Yi, W. & Xue, P. Manipulating directional flow in a two-dimensional photonic quantum walk under a synthetic magnetic field. *Nat. Commun.* **14**, 6283 (2023).
37. Zheng, X. et al. Dynamic control of 2D non-Hermitian photonic corner skin modes in synthetic dimensions. *Nat. Commun.* **15**, 10881 (2024).
38. Muniz, A. L. M. et al. Observation of photon-photon thermodynamic processes under negative optical temperature conditions. *Science* **379**, 1019-1023 (2023).
39. Dinani, H. M. et al. Universal routing of light via optical thermodynamics. *Nat. Photon.* **19**, 1116-1121 (2025).
40. Wang, S. et al. Nonlinear non-Hermitian skin effect and skin solitons in temporal photonic feedforward lattices. *Phys. Rev. Lett.* **134**, 243805 (2025).
41. Weidemann, S., Kremer, M., Longhi, S. & Szameit, A. Coexistence of dynamical delocalization and spectral localization through stochastic dissipation. *Nat. Photon.* **15**, 576-581 (2021).

42. Longhi, S. Dephasing-induced mobility edges in quasicrystals. *Phys. Rev. Lett.* **132**, 236301 (2024).
43. Longhi, S. Incoherent non-Hermitian skin effect in photonic quantum walks. *Light Sci. Appl.* **13**, 95 (2024).

Acknowledgements

The work was supported by the National Key Research and Development Program of China (grant no. 2025YFA1411800), the National Natural Science Foundation of China (grant nos. U25D8017, 12374305, and 12474381), the European Research Council grant EmergenTopo (865151), the CDP C2EMPI, as well as the French State under the France-2030 programme, the University of Lille, the Initiative of Excellence of the University of Lille, the European Metropolis of Lille (R-CDP-24-004-C2EMPI).

Author contributions

B. W. supervised the project. B. W., C. Q. and P. L. conceived the study and designed the experiment. C. Q. and Y. L. performed the experiment. J. X. and M. Z. assisted the experiment. B. W., C. Q., Y. L., M. Z. and X. H. analyzed the data. C. Q., B. W. and A. A. performed the theoretical analysis. B. W. and C. Q. performed the numerical simulations and co-wrote the manuscript. All authors discussed the results and commented on the manuscript.

Competing interests

The authors declare no competing interests.

Additional information

Figures and captions

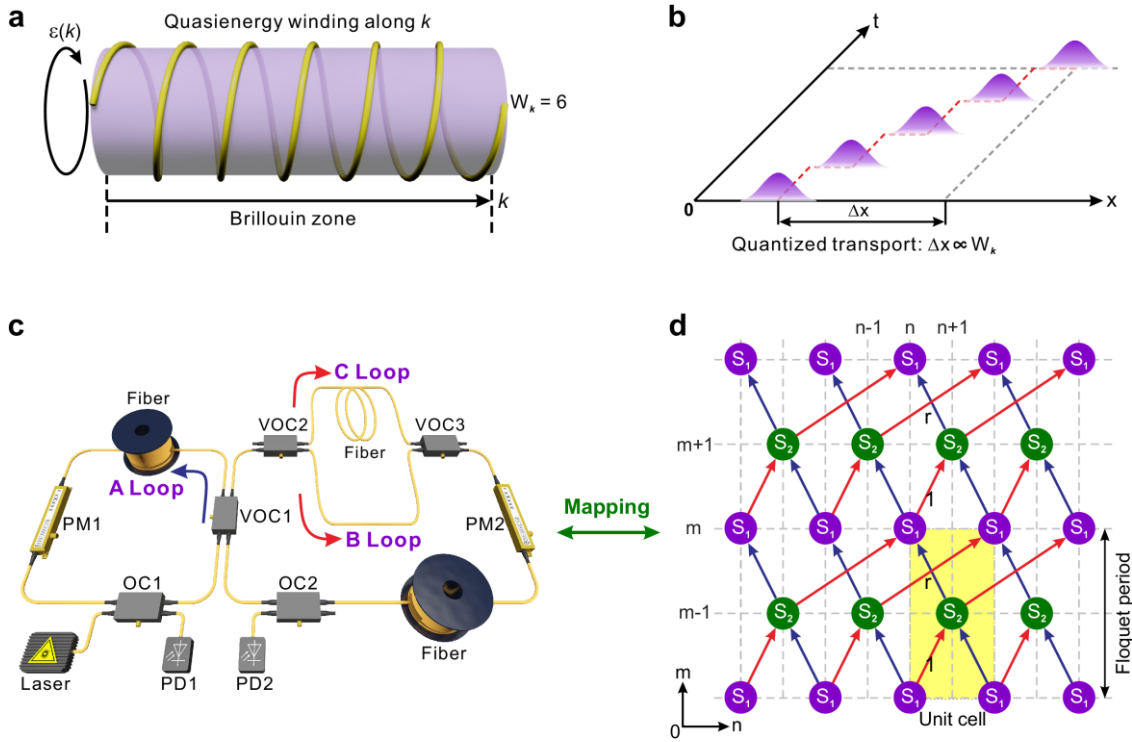


Fig. 1 | Physical picture, triple fiber-loop circuit and equivalent quantum walk. **a** Physical picture of the quasienergy winding along the k direction with integer winding number $W_k = 6$. **b** Schematic of quantized transport with integer displacement of $\Delta x \propto W_k$. **c** Schematic of a triple fiber-loop circuit consisting of a shorter A loop and two longer B, C loops. Main optical components include laser source, phase modulator (PM), optical coupler (OC), variable optical coupler (VOC) and fibers. **d** Equivalent temporal quantum walk formed by mapping from pulse evolution in triple fiber loops. Pulse circulation in A, B/C loops can be mapped into leftward, rightward propagation links, and pulse splitting at central VOC corresponds to scattering at the node. By precisely designing loop lengths and making pulse pass through B/C loops at odd/even steps, one can realize alternate rightward nearest and r -th order long-range couplings. The rectangular shaded region denotes one Floquet period consisting of two steps.

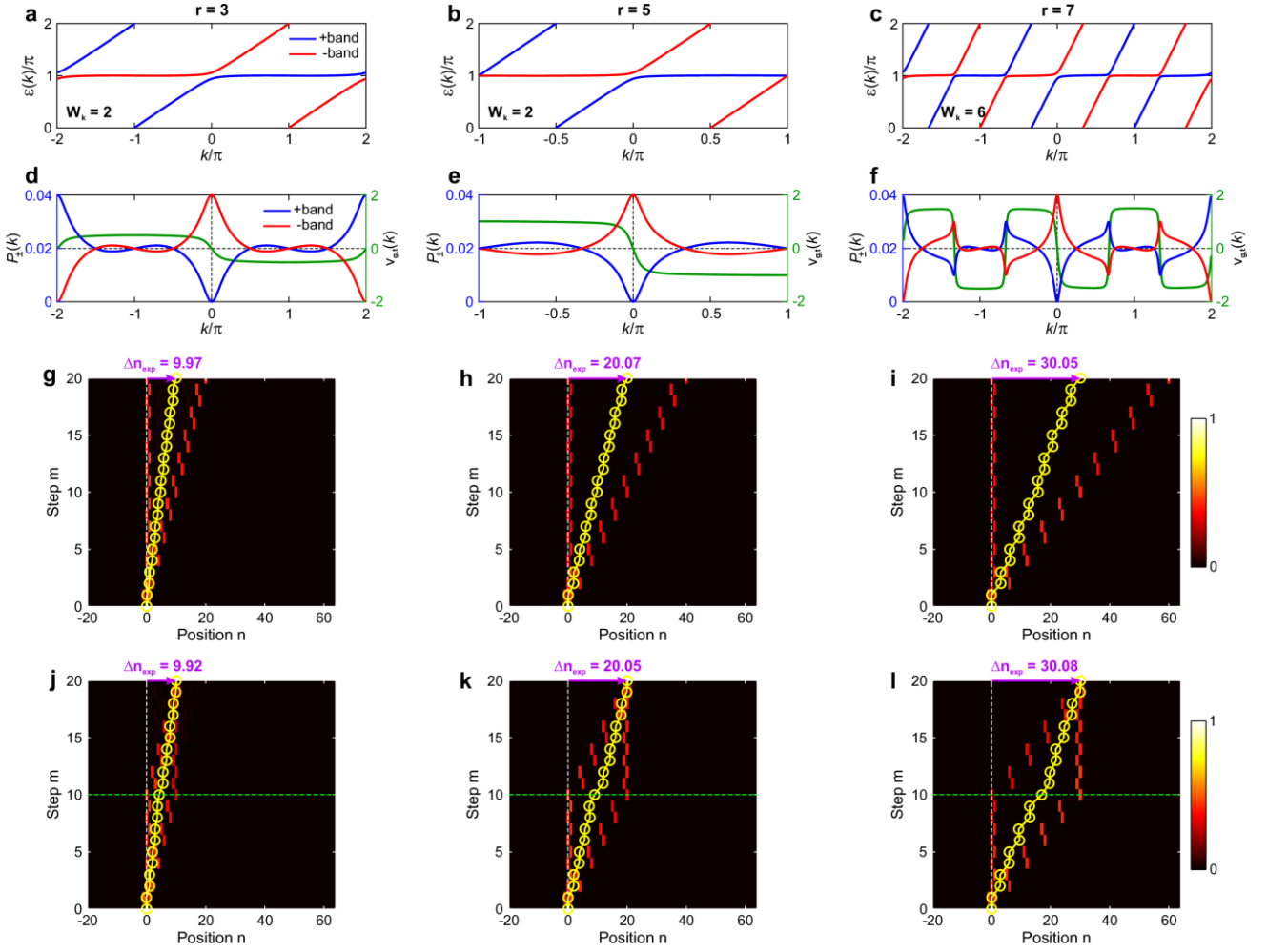
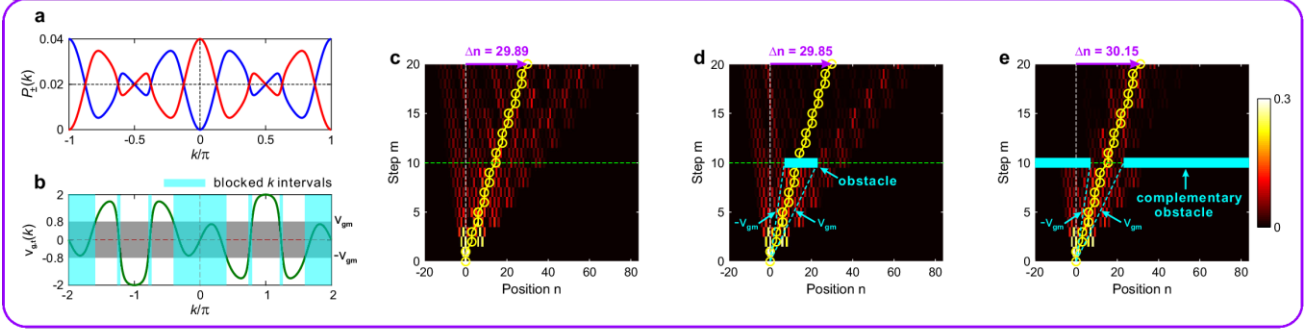


Fig.2| Band structures, band excitation probabilities, group velocities and field evolutions for three long-range coupling orders $r = 3, 5, 7$. **a-c** Calculated Floquet band structures for $r = 3, 5, 7$, showing $K = 4\pi, 2\pi, 4\pi$ and $W_k = 2, 2, 6$ where $\beta_{1,2} = 0.47\pi$. **d-f** Normalized excitation probabilities of $P_{\pm}(k)$ with normalization condition $\int_{-K/2}^{K/2} [P_+(k) + P_-(k)] dk = 1$ and group velocities $v_{g,\pm}(k)$. **g-i** Field diffraction patterns under single-site inputs, with yellow circles denoting the extracted beam COM. The COM displacements in 20 steps ($P = 10$ Floquet periods) are $\Delta n_{\text{exp}} = 9.97, 20.07, 30.05$. **j-l** Field refraction processes for $r = 3, 5, 7$, showing COM displacements of $\Delta n_{\text{exp}} = 9.92, 20.05, 30.08$.

robust against obstacles



robust against disorders

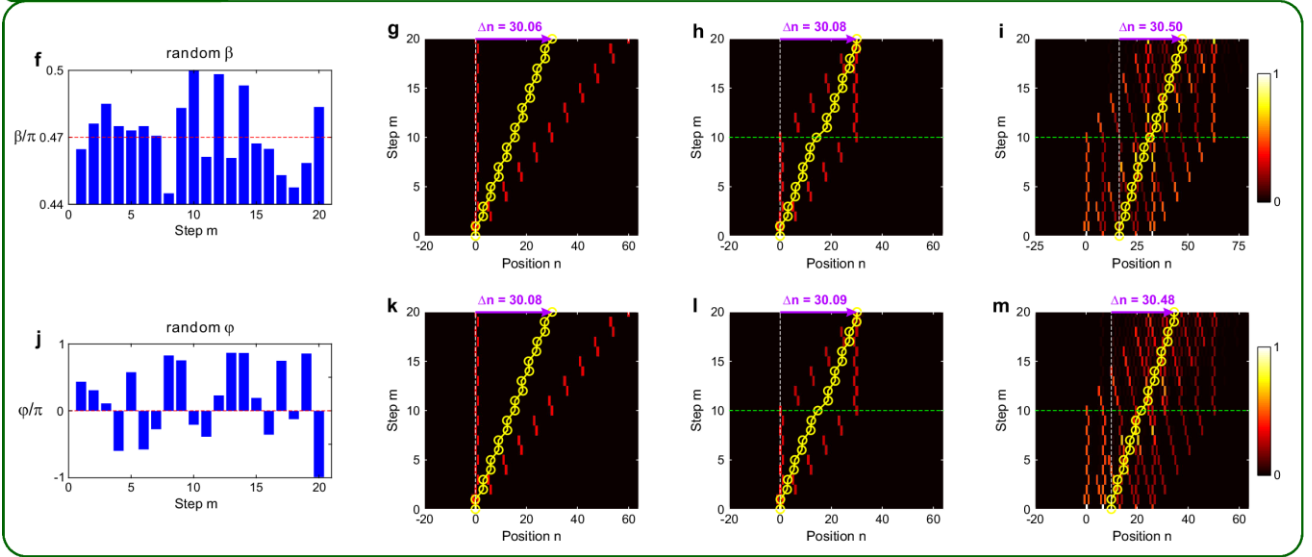


Fig. 3| Robustness properties of quantized transport against obstacles and disorders. **a** Band excitation probabilities $p_{\pm}(k)$ for $r = 7$, $\beta_{1,2} = \pi/4$. **b** Group velocity $v_{g,i}(k)$ showing symmetrically-distributed blocked intervals denoted by the cyan ribbons. **c-e** Field diffraction patterns for three cases: **(i)** without obstacle; **(ii)** with a symmetric obstacle at $m = M/2 = 10$ step with width $\Omega = 16$ and **(iii)** with a complementary symmetric obstacle. The obstacle in **(ii)** corresponds to the blocked intervals in the BZ. **f** Schematic of a randomly varying coupling angle $\beta(m) = \beta_0 + \Delta\beta(m)$, where $\beta_0 = 0.47\pi$, $\Delta\beta(m) \in [-0.3\pi, 0.3\pi]$ with a uniform probability. **g-i** Measured field diffraction and refraction patterns for single-site and multi-site inputs under the random $\beta(m)$. **j** Schematic of a randomly varying scalar potential $\varphi(m) \in [-\pi, \pi]$ with a uniform probability (see Supplementary Section 2 for more detailed analysis). **k-m** Measured field diffraction and refraction patterns under single-site and multi-site inputs in the presence of random $\varphi(m)$.

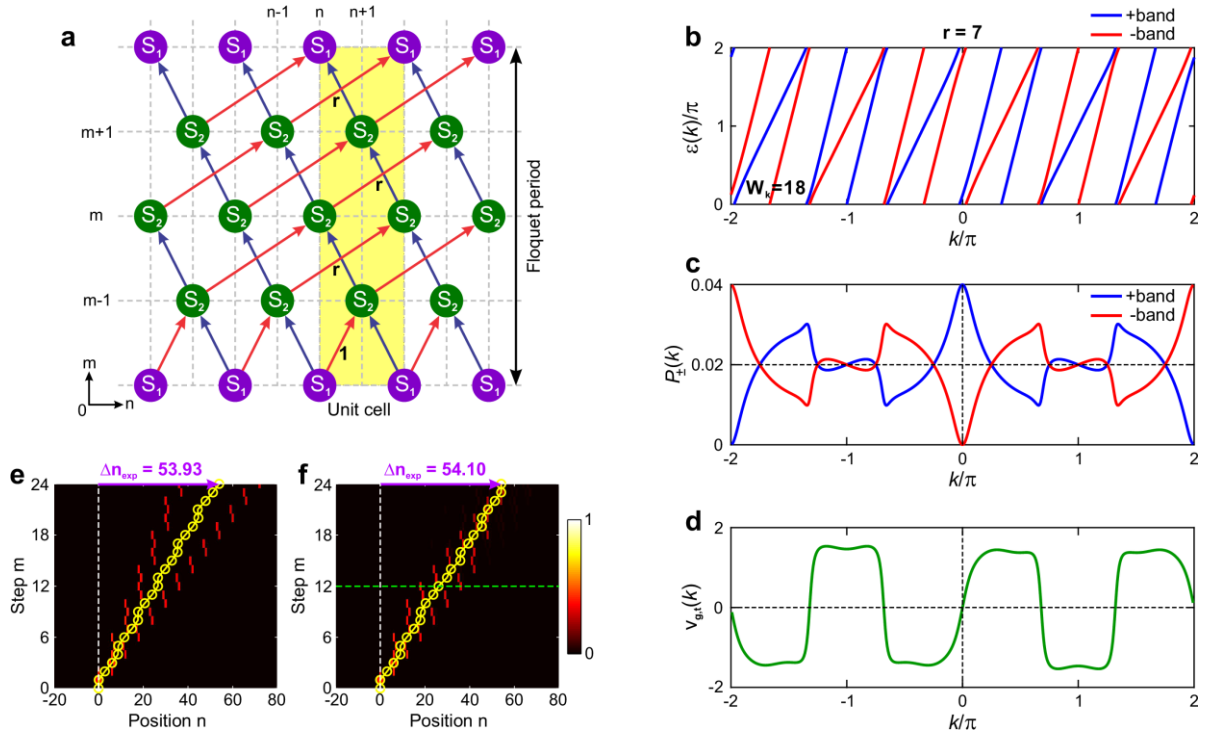


Fig. 4| Quantum-walk structure, band structure, band excitation probability and field evolutions for multi-step driving case. a Schematic of a four-step-driving quantum walk with coupling orders $r_i = 1, r, r, r$ in one Floquet period. **b** Floquet band structure for $r = 7$, which manifest as $K = 4\pi$ and $W_k = 18$. **c, d** Calculated $P_{\pm}(k)$ and $v_{g,t}(k)$ in the BZ. **e, f** Measured field diffraction and refraction patterns under single-site input, showing COM displacements of $\Delta n_{\text{exp}} = 53.93, 54.10$.

Methods

Experimental setup

The layout of experimental setup is shown in Extended Data Fig. 1, which consists of triple coupled fiber loops (denoted by A, B, C) and an input module. In the input module, a 1555 nm continuous laser beam is cut into a ~ 110 ns duration seed pulse via a Mach-Zehnder modulator (MZM) and then injected into A loop via an optical coupler (OC). The pulse will undergo periodic splitting and interference at central variable optical coupler (VOC1) and path selection between B/C loops at odd/even circulating trips via VOC2, VOC3 to form a temporal quantum walk with alternate nearest/long-range couplings. The splitting ratios of three VOCs are controlled by programmed gate voltages driving by the arbitrary waveform generators (AWGs). According to the relation between long-range coupling order r and loop lengths, $(L_C - L_A)/(L_B - L_A) = (r+1)/(1+1)$, to achieve $r = 3, 5, 7$, we choose $L_A \sim 5\text{km}$, $L_B \sim 5\text{km} + 35\text{ m}$, $L_C \sim 5\text{km} + 70\text{ m}$, $5\text{km} + 105\text{ m}$, $5\text{km} + 140\text{ m}$. The lengths correspond to a mean pulse travel time $T_m \sim 25\text{ }\mu\text{s}$ in each loop and a pulse interval of $\Delta t \sim 175\text{ ns}$ by propagating in A/B loops and $\Delta t \sim 350\text{ ns}$, 525 ns , 700 ns in A/C loops for $r = 3, 5, 7$ cases. More precise control over the loop lengths is discussed below. The two characteristic times T_m and $\Delta t/2$ define the time slots in the m and n axes of temporal quantum walk. Note that the duration time of seed pulse is shorter than the pulse interval Δt , ensuring no crosstalk between adjacent pulses. Erbium-doped fiber amplifiers (EDFAs) are used to compensate for the device insertion losses and coupling losses in the loops. To overcome the influence of transient response of EDFA, a high-power 1538 nm continuous-wave laser light is introduced before each EDFA. After passing the EDFA, a band-pass filter (BPF) is used to remove the control light to eliminate the spontaneous emission noise. Polarization controllers (PCs) and polarization beam splitter (PBS) are utilized to control the polarization states of light pulses. Acoustic optical modulators (AOMs) serve as absorbers to remove the pulse train after hundreds of circulations. Optical couplers (OCs) are utilized to couple a portion ($\sim 1\%$) of pulses out of the loops for detection by photodiodes (PDs).

Methods to realize precise control over the loop lengths

To achieve more precise control over the loop lengths, we perform repeated pulse interval measurement and loop length adjustment using compensated fiber segments. Firstly, we tune the splitting ratios of VOC2, VOC3 to 1:0 to select the B loop path. By setting the coupling angle of VOC1 to $\beta = \pi/4$ and

injecting a single pulse from A loop, the pulse will evolve into a pulse train by circulating in A/B loops, whose distributions at each step are shown in Extended Data Fig. 2a. From the pulse distribution within a specific step (for example at $m = 2$ step denoted by the zoom in figure below), we can measure the peak-to-peak pulse interval of $\Delta t_1 = 176.16$ ns, which sets the basic time slot of $dn = \Delta t_1/2$ along the n axis for the nearest-neighbor coupling $r = 1$. Then, we tune the splitting ratios of VOC2, VOC3 to 0:1 to select the C loop path. With similar procedures, we can obtain three pulse intervals of $\Delta t_2, \Delta t_3, \Delta t_4$ for $r = 3, 5, 7$. For example for $r = 3$, at initial choice of C loop length, the condition $\Delta t_2/\Delta t_1 = (r+1)/(1+1) = 2$ is usually not precisely satisfied. Then we adjust the length of C loop by adding and cutting down the fiber segments and measuring the pulse interval again. After repeated pulse interval measurement and loop length adjustment, we can approach the loop length condition as precise as possible. More exactly, we record the pulse sequences in B and C loops together in the oscilloscope. When the pulse sequence in C loop can overlap with that in the B loop every other one with negligible offset, we judge the loop length condition is satisfied with a sufficient precision. In our measurement, we finally obtain $\Delta t_2 = 354.08$ ns, $\Delta t_3 = 529.92$ ns, $\Delta t_4 = 706.08$ ns (see Extended Data Figs. 2b-2d), with $\Delta t_2 = 2\Delta t_1 + 1.76$ ns, $\Delta t_3 = 3\Delta t_1 + 1.44$ ns, $\Delta t_4 = 4\Delta t_1 + 1.44$ ns. Note that the deviations (offsets) are at the scale of 1~2 ns that are much shorter than $\Delta t_{1,2,3,4}$ and pulse duration time itself (~ 110 ns), being sufficient to fulfill the loop length condition. We further verify the length condition is sufficiently fulfilled by monitoring the results. When we increase the precision by further cutting down or adding fiber segments, we find the precision of quantized transport displacement can't be improved any more. Then we judge that the loop length condition is satisfied sufficiently. Finally, it is worth noting that the residual length mismatch will bring about an additional phase shift into C loop at even steps, which is equivalent to the introduction of an additional vector potential. The additional phase shift is compensated using PM outside the B, C loops. More details about phase compensation are discussed in the following section.

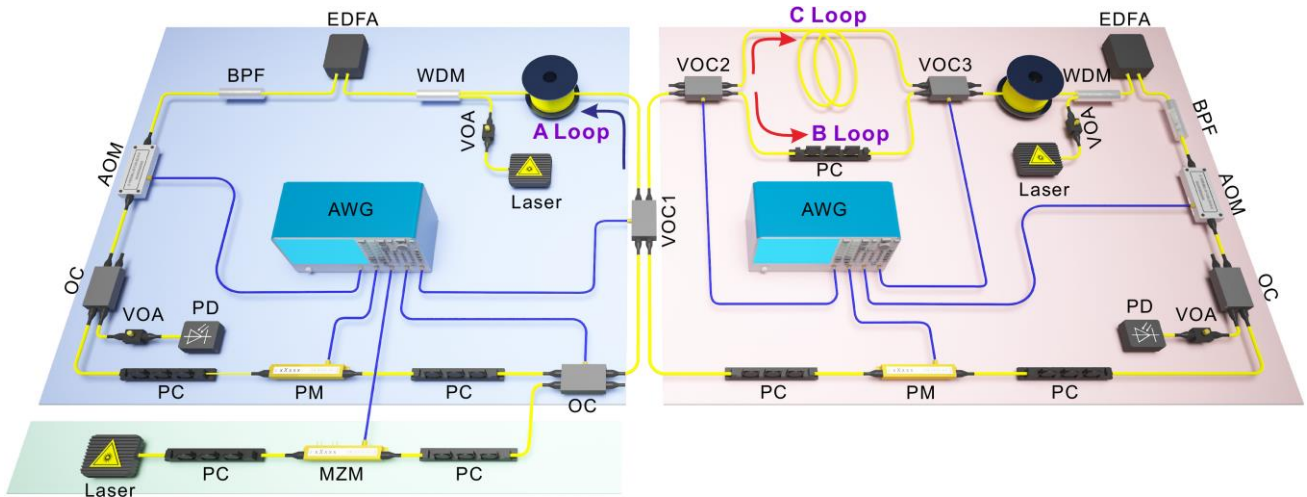
Methods to ensure vanishing phase shifts in the propagation paths of lattice

Here we discuss how to achieve the vanishing phase shifts along the propagation paths. Firstly, to make the real parts of phase shifts vanish, we turn off all PMs in three loops to eliminate propagation phases. Note that there exists an additional phase shift of $\pi/2$ accompanying the cross-arm optical coupling in VOC2 and VOC3 when the C loop is selected, giving rise to a total phase shift of π in C loop compared to that in B loop. Also, the residual loop length mismatch will bring about an additional unknown phase

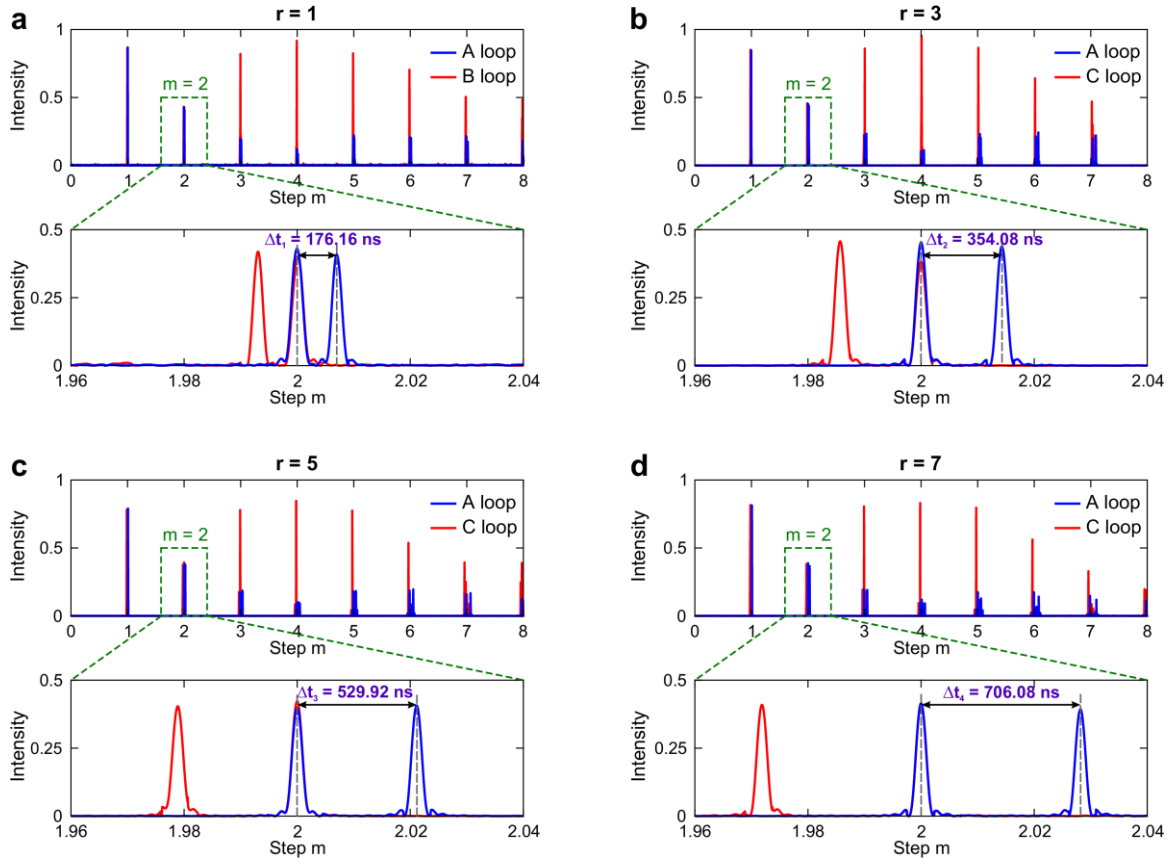
shift in C loop. We firstly apply a gate voltage of V_π in the PM in the common circuit of B, C loops at even steps to compensate for the fixed π phase shift. The additional length-mismatch induced phase shift is compensated by monitoring the field evolutions. We tune the additional phase until we achieve the most precise quantized transport displacement, indicating that the phase shift is well compensated. Secondly, to make the imaginary parts of phase shifts vanish, we combine EDFAs and PCs to precisely control the gain/loss rates in the three loops. By monitoring the pulse intensities evolution in all steps, we can tune EDFAs and PCs in real time until a vanishing net gain/loss between adjacent steps is achieved. Also, due to the distinct lengths of B, C loops and different device insertion losses in the two paths, a PC is incorporated into B loop to realize fine tuning of the gain/loss to reach a balanced state.

Methods to realize single-site $1:\pm 1$ input condition from two loops

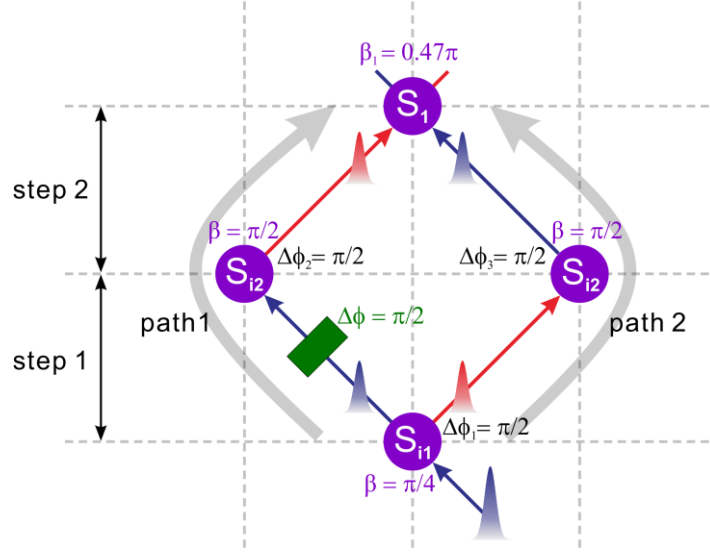
As discussed in the main text, a required condition for the quantized transport is to realize 1:1 or 1:-1 single-site input from two loops. This can be realized by applying two preprocessed steps before $m = 0$ steps (see Extended Date Fig. 3). In the first step, we set the coupling angle as $\beta = \pi/4$ and inject a single pulse from the short loop at $n = 0$ site, which will give rise to 1:1 equal-amplitude pulse splitting. During the pulse splitting process, the pulse propagating through the cross arm of VOC1 will acquire a phase shift of $\Delta\phi_1 = \pi/2$. In the second step, by setting the coupling angle as $\beta = \pi/2$ with 1:0 splitting ratio, we can achieve total pulse transfer from short (long) to long (short) loop, accompanied by an additional phase shift of $\Delta\phi_2 = \Delta\phi_3 = \pi/2$. To guarantee a total phase difference of 0 or π between the two paths (path 1 and path 2), we insert an additional phase shift of $\Delta\phi = \pi/2$ into short loop in the first step to compensate this unbalanced phase shift.



Extended Data Fig.1| Layout of the experimental setup. Optical components include: MZM, Mach-Zehnder modulator; PM, phase modulator; SMF, single mode fiber; PC, polarization controller; AOM, acousto-optic modulator; OC, optical coupler with constant splitting ratio; VOC, variable optical coupler with programable splitting ratio; EDFA, erbium-doped fiber amplifier; PD, photodiode; VOA, variable optical attenuator; WDM, wavelength division multiplexer; BPF, band-pass filter. Radio frequency components include: OSC, oscilloscope; AWG, arbitrary waveform generator.



Extended Data Fig.2 | Measured pulse intervals for different coupling order of $r = 1, 3, 5, 7$. In **a-d**, the pulse intervals are $\Delta t_1 = 176.16$ ns, $\Delta t_2 = 354.08$ ns, $\Delta t_3 = 529.92$ ns, $\Delta t_4 = 706.08$ ns. The blue and red curves denote the pulse distributions in A and B/C loops. The zoom in figure in each panel shows the pulse distributions at $m = 2$ step.



Extended Data Fig. 3| Schematic of two preprocessed steps to realize single-site 1:±1 input from two loops. The coupling angles in step 1 and step 2 are set as $\beta = \pi/4$ and $\beta = \pi/2$, giving rise to equal-amplitude pulse splitting and total pulse transfer from short (long) to long (short) loop. The additional phase shifts accompanying cross-arm light couplings are $\Delta\phi_1 = \Delta\phi_2 = \Delta\phi_3 = \pi/2$. To reach balanced phase shifts in the two paths, in the first step we insert an additional phase shift of $\Delta\phi = \pi/2$ into A loop.